Shear Alfvén continua in stellarators

D. A. Spong
Oak Ridge National Laboratory, P.O. Box 2009, Oak Ridge, Tennessee 37831-8071

R. Sanchez
Universidad Carlos III de Madrid, Madrid, Spain

A. Weller
Max-Planck-Institut für Plasmaphysik, IPP-Euratom, Garching, Germany

(Received 14 January 2003; accepted 15 May 2003)

Shear Alfvén continua have been calculated for stellarators over a range of shapes and aspect ratios as a first step toward understanding Alfvén instability induced fast ion losses in such systems and possible means for minimizing these losses. Stellarators introduce strong poloidal/toroidal couplings in both $|B|$ and the $g^{\rho\rho}$ metric coefficient that can induce new continuum gap structures not present in axisymmetric tokamaks. Low field period ($N_{\mathrm{fp}}=2-3$), low aspect ratio devices result in strongly coupled toroidal mode families ($n=\pm n_0, \pm n_0 \pm N_{\mathrm{fp}}, \pm n_0 \pm 2N_{\mathrm{fp}}$, etc.) that lead to helically coupled Alfvén gaps at lower frequencies and with wider gap structures than are the case for larger aspect ratio, higher field period stellarator devices. © *2003 American Institute of Physics.*
[DOI: 10.1063/1.1590316]

I. INTRODUCTION

Fast ion destabilized Alfvén modes[1,2] are of interest in stellarators,[3–10] since they can lead to enhanced fast ion losses and lowered heating efficiencies. In addition, these instabilities have potential diagnostic use[11] [MHD (magnetohydrodynamics) spectroscopy], and may offer the possibility of directly channeling[12] fast ion energy to core ions through wave-particle mechanisms (i.e., bypassing the slower collisional transfer mechanisms). Optimized stellarators also offer the possibility of controlling the severity of Alfvén modes through the tailoring of the plasma shape.

Recently, there has been significant interest in the design of compact stellarators; these offer the potential of larger confined plasma volumes at fixed capital cost while preserving steady-state operation along with good confinement and stability properties. However, low aspect ratio stellarators have stronger poloidal/toroidal/helical couplings in $|B|$ and the $g^{\rho\rho}$ metric coefficient than either tokamaks or large aspect ratio stellarators. These couplings are caused by the requirements that the magnetic field and metric elements be periodic functions in both poloidal and toroidal angles; this periodicity leads to the appearance of gap modes in an analogous way to those encountered in periodic lattice structures in condensed matter physics. Since the Alfvén gaps arise out of the couplings present in the function $g^{\rho\rho}/|B|^2$, low aspect ratio devices can have wider gap structures than high aspect ratio configurations. Also, low aspect ratio devices are generally designed at low field periods ($N_{\mathrm{fp}}=2-3$); as a result, more closely spaced toroidal mode families must be taken into account in calculating the Alfvén spectrum. Calculations have recently been made of Alfvén continua for large aspect ratio stellarators.[5,6,9] In order to analyze Alfvén continua in low aspect ratio devices and to make contact with large aspect ratio results, we have developed a computational tool (the STELLGAP code) that can take into account interactions between multiple toroidal modes while retaining an adequately resolved Fourier spectrum for the equilibrium quantities. This code utilizes MPI (message passing interface) parallelism over flux surfaces in order to allow both a high degree of radial and Fourier space resolution.

In the following, Alfvén continuum structures will be surveyed in both large and small aspect ratio stellarators. Calculation of the Alfvén continuum structure is the first step in predicting the frequency spectrum and stability properties of energetic particle destabilized modes in stellarators. Discrete modes with a global radial extent generally exist in the gaps between adjacent Alfvén continua; these discrete modes can be destabilized by energetic particles through inverse Landau damping[2] when the fast particle velocity matches either the phase velocity of the stable discrete mode ($\sim v_A$) or its coupled sidebands[13] ($\leqslant v_A$). When such instabilities are near marginal stability, it is expected that if the mode's real frequency matches the frequency of neighboring continua, continuum damping will result, increasing the threshold of the energetic particle pressure gradient required to drive these modes unstable. Studies of such effects in tokamaks have shown good correlations between analytical continuum damping predictions[14] and non-perturbative numerical calculations[15] of Alfvén mode stability.

As a result of their three-dimensional (3D) shaping, stellarators offer a higher degree of design flexibility than tokamaks. Over the past few years, comprehensive physics/engineering based design tools have been developed[16] that allow the optimization of stellarators with respect to confinement, stability, equilibrium robustness and a range of magnet coil engineering issues. It is expected that the model developed in this paper could ultimately be applied as an additional target for such optimizations. Due to the fact that the Alfvén continuum structure is determined by the geometric and $|B|$ couplings, and that these can be directly influenced

 © 2003 American Institute of Physics

Downloaded 27 Jan 2004 to 160.91.248.206. Redistribution subject to AIP license or copyright, see http://ojps.aip.org/pop/popcr.jsp

by plasma shaping, it is anticipated that stellarators could be optimized in ways that could enhance continuum damping effects over at least limited ranges of frequency.

In the following sections, we first present the Alfvén continuum equation, describe the solution techniques appropriate to 3D systems, and outline the categories of Alfvén gaps that can be addressed with this calculation (Sec. II). Next, in Sec. III, our model is applied to several examples of large aspect ratio stellarator configurations. In Sec. IV, we analyze Alfvén continua for two recent low aspect ratio devices having quasi-poloidal and quasi-toroidal symmetries. Finally, in Sec. V we present our conclusions.

II. ALFVÉN CONTINUUM EQUATIONS AND SOLUTION TECHNIQUE

The Alfvén continuum equation[17] for 3D stellarator equilibria in the low β, incompressible limit (i.e., no sound wave coupling) can be written as follows:

$$\mu_0\rho\omega^2\frac{|\nabla\psi|^2}{B^2}E_\psi+\mathbf{B}\cdot\nabla\left\{\frac{|\nabla\psi|^2}{B^2}(\mathbf{B}\cdot\nabla)E_\psi\right\}=0, \tag{1}$$

where E_ψ is the covariant ψ component of electric field. We have solved the above equation in straight field line Boozer coordinates.[18] The use of straight field line coordinates preserves the zeros of the $\mathbf{B}\cdot\nabla$ operator when coupled with a Fourier series representation for E_ψ:

$$E_\psi=\sum_{j=1}^{L}E_\psi^j e_j \quad \text{where} \quad e_j=\cos(n_j\zeta-m_j\theta). \tag{2}$$

For the calculation of Alfvén continua in devices with stellarator symmetry, one can consider the cosine and sine components separately in the Fourier expansion of E_ψ (due to the fact that they are not coupled). Since both have been found to lead to similar continua, we will consider only the cosine expansion of E_ψ in this paper. An exact representation of the $\mathbf{B}\cdot\nabla$ operator has been found necessary to preserve the zero frequency crossings (that occur at mode rational surfaces) of the lowest frequency shear Alfvén continuum. The above equation can be expressed in Boozer coordinates using the following relations:

$$\mathbf{B}\cdot\nabla=\frac{1}{\sqrt{g}}\left(\iota\frac{\partial}{\partial\theta}+\frac{\partial}{\partial\zeta}\right) \quad \text{and} \quad |\nabla\psi|^2=g^{\rho\rho}\left(\frac{d\psi}{d\rho}\right)^2, \tag{3}$$

where θ is the poloidal coordinate, ζ is the toroidal coordinate, ρ is the normalized flux surface label, $g^{\rho\rho}$ is the contravariant $\rho\rho$ metric element and ι is the rotational transform.

Multiplying Eq. (1) by $\sqrt{g}\cos(n_i\zeta-m_i\theta)$ and flux surface averaging, denoted by $\langle\cdots\rangle=\int_0^{2\pi}d\zeta\int_0^{2\pi}d\theta(\cdots)$ where $\sqrt{g}$ is the Jacobian, we obtain

$$\mu_0\omega^2\rho\left\langle e_i\sqrt{g}\,\frac{g^{\rho\rho}}{B^2}\sum_{j=1}^{L}E_\psi^j e_j\right\rangle+\left\langle e_i\left(\iota\frac{\partial}{\partial\theta}+\frac{\partial}{\partial\zeta}\right)\times\frac{g^{\rho\rho}}{B^2\sqrt{g}}\left(\iota\frac{\partial}{\partial\theta}+\frac{\partial}{\partial\zeta}\right)\sum_{j=1}^{L}E_\psi^j e_j\right\rangle=0. \tag{4}$$

The second term in the above equation can then be integrated by parts to obtain the following symmetric matrix eigenvalue equation:

$$\omega^2\overleftrightarrow{A}\mathbf{x}=\overleftrightarrow{B}\mathbf{x}$$

$$\text{where } \overleftrightarrow{A}=[a_{ij}]=\mu_0\rho\left\langle e_i\sqrt{g}\frac{g^{\rho\rho}}{B^2}e_j\right\rangle,$$

$$\overleftrightarrow{B}=[b_{ij}]=\left\langle\frac{g^{\rho\rho}}{B^2\sqrt{g}}\left(\iota\frac{\partial e_i}{\partial\theta}+\frac{\partial e_i}{\partial\zeta}\right)\left(\iota\frac{\partial e_j}{\partial\theta}+\frac{\partial e_j}{\partial\zeta}\right)\right\rangle,$$

$$\mathbf{x}=[E_\psi^1\,E_\psi^2\,E_\psi^3\cdots E_\psi^L]^T. \tag{5}$$

These matrix elements are obtained after expanding the following products of magnetic field components and metric elements in terms of Fourier series:

$$\frac{g^{\rho\rho}\sqrt{g}}{B^2}=\sum_{k=1}^{K}E_k\cos(n_k\zeta-m_k\theta),$$
$$\frac{g^{\rho\rho}}{B^2\sqrt{g}}=\sum_{k=1}^{K}F_k\cos(n_k\zeta-m_k\theta). \tag{6}$$

The quantities on the left hand side of the above equations are initially calculated for each flux surface on a mesh in θ and ζ by forming the appropriate products and quotients of equilibrium quantities. These data are then transformed to a Fourier space representation, keeping the shortest Fourier wavelength at least a factor of 2–3 larger than the mesh spacing to avoid anti-aliasing errors. The matrix elements then depend on two convolution integrals [other Fourier product combinations such as those involving $\cos(n_i\zeta-m_i\theta)\sin(n_j\zeta-m_j\theta)\cos(n_k\zeta-m_k\theta)$ and $\sin(n_i\zeta-m_i\theta)\sin(n_j\zeta-m_j\theta)\sin(n_k\zeta-m_k\theta)$ integrate to 0]:

$$I_{ccc}^{i,j,k}=\int_{-\pi}^{\pi}d\zeta\int_{-\pi}^{\pi}d\theta\cos(n_i\zeta-m_i\theta)\cos(n_j\zeta-m_j\theta)\times\cos(n_k\zeta-m_k\theta),$$
$$I_{ssc}^{i,j,k}=\int_{-\pi}^{\pi}d\zeta\int_{-\pi}^{\pi}d\theta\sin(n_i\zeta-m_i\theta)\sin(n_j\zeta-m_j\theta)\times\cos(n_k\zeta-m_k\theta). \tag{7}$$

Analytic algorithms have been developed to provide these integrals for arbitrary combinations of the mode numbers m_i, n_i, m_j, n_j, m_k, n_k. The calculation of similar integrals has been discussed previously in Ref. 19. The required matrix elements may then be written as

$$a_{ij}=\mu_0\rho_{ion}\sum_{k=1}^{K}I_{ccc}^{i,j,k}E_k,$$
$$b_{ij}=\sum_{k=1}^{K}I_{ssc}^{i,j,k}F_k[\iota^2m_im_j+n_in_j+\iota(m_in_j+m_jn_i)]. \tag{8}$$

Equation (1) has thus been reduced to a symmetric matrix eigenvalue problem. We solve the above system of equations for all possible eigenvalues and eigenfunctions using the DGEGV routine from the IBM ESSL library.[20] It is expected that a higher performance continuum calculation (such as

Downloaded 27 Jan 2004 to 160.91.248.206. Redistribution subject to AIP license or copyright, see http://ojps.aip.org/pop/popcr.jsp

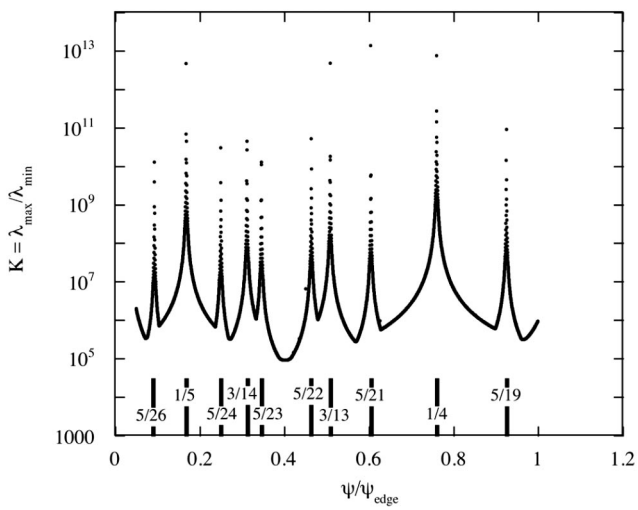

FIG. 1. Condition number vs flux surface location for a 2 field period QPS configuration showing alignment of the peaks in condition number with rational surfaces.

might be required for a stellarator optimization) can be developed by calculating only a subset of the eigenvalues of the above equations (e.g., only for lower frequencies). The numerical accuracy of the eigenvalues obtained from solving Eq. (1) has been evaluated by calculating the condition number of the linear system. This represents the degree to which errors in the original matrix elements are magnified in the process of computing eigenvalues. The condition number is estimated here by taking the ratio of the largest eigenvalue to the smallest eigenvalue. Since the smallest eigenvalue will go to zero at rational surfaces, large condition numbers are expected in these regions. In Fig. 1 we plot the condition number vs flux surface for the low aspect ratio quasi-poloidal stellarator case discussed in the next section. Since these calculations are all performed in double precision, condition numbers less that about 10^{12} should still provide greater than 3–4 significant figures in the final answers. Since no further processing of these results is made, this is adequate for the present purposes. We have found in earlier versions of this calculation that attempted to use finite differencing (which gives an inexact representation for the parallel gradient operator) rather than the currently used Fourier representation, ill-conditioning was much more dominant and resulted in badly distorted continua. It is also noted that close to rational surfaces the introduction of other physics (i.e., compressibility, dissipative effects, kinetic effects, etc.) may moderate the tendency towards ill-conditioning that is characteristic of ideal MHD.

We have solved Eq. (1) for a variety of different stellarator configurations. Due to the absence of toroidal symmetry, the toroidal mode number, n, is no longer a good quantum number; a range of n's must be included in the representation for the Alfvén eigenfunction, E_ψ. However, since this is a linear problem, the toroidal mode numbers that are of relevance are limited to those that are displaced from the initial n by an integer times the number of field periods. We have adopted the mode selection convention here that the poloidal mode numbers are positive; there must then be both positive and negative n's present. For example, in an axisymmetric system one would represent E_ψ with $n=\pm n_0$, and $m=0$ to $m_{\max}$. For a stellarator the n's must be augmented with sidebands at $n_0 \pm N_{\mathrm{fp}}$, $n_0 \pm 2N_{\mathrm{fp}}$, etc., as well as at $-n_0 \pm N_{\mathrm{fp}}$, $-n_0 \pm 2N_{\mathrm{fp}}$, etc. In the following we refer this to as the $n=n_0$ mode family. In some cases for low field period stellarators (i.e., when $n_0 = N_{\mathrm{fp}}/2$) the $+n_0$ and $-n_0$ series will overlap so that only $n = n_0 \pm N_{\mathrm{fp}}$, $n_0 \pm 2N_{\mathrm{fp}}$,... terms are required. For each toroidal mode number, a set of positive poloidal modes are included up to some maximum m value. For the examples given below, we have represented E_ψ using 6–8 toroidal modes and a sufficient range of poloidal modes so as to include those helicities present in the rotational transform profile ($n/\iota_{\max} < m < n/\iota_{\min}$) as well as to accommodate Alfvén couplings from adjacent toroidal modes. For most configurations, the negative helicity modes ($n/m<0$) result in Alfvén continua only at relatively high frequencies [i.e., $\omega_A \approx v_A(n+\iota m)/R$] in comparison to the positive helicity modes which are more dominant at low frequencies [i.e., $\omega_A \approx v_A(n-\iota m)/R$]. The equilibrium coefficients are typically represented by 20 poloidal modes and 20 toroidal modes and we calculate Alfvén continua for 2048 surfaces. Isolated tests have been made using a greater number of equilibrium modes and have indicated no substantial change in the results. This model can also be applied with only a single $n=n_0$ toroidal mode number present in the representation for E_ψ. This is effectively a tokamak limit in that only the $n=0$ terms in the equilibrium will then contribute to the matrix elements of Eq. (8).

There are a number of different categories of Alfvén gaps that are of interest in stellarators. These gaps are formed when the parallel wave numbers match between two oppositely propagating shear Alfvén waves whose toroidal and poloidal mode numbers differ by spacings corresponding to modes that are present in the underlying equilibrium. This condition can be expressed in a simple cylindrical model as:

$$k_{\parallel,m,n} = -k_{\parallel,(m+\delta_m),(n+\delta_n N_{\mathrm{fp}})}$$

$$\text{or} \quad n - m\iota = -(n + \delta_n N_{\mathrm{fp}} - m\iota - \delta_m \iota)$$

where n, m = toroidal and poloidal mode numbers

δ_m, δ_n = integer mode displacements (can be positive or negative)

ι = rotational transform, N_{fp} = field periods.

Solving for the gap location (expressed here in terms of the rotational transform) and frequency, results in

$$\iota = \frac{2n + \delta_n N_{\mathrm{fp}}}{2m + \delta_m}, \quad \omega = \left(\frac{v_A}{R}\right) \frac{\delta_m n - \delta_n m N_{\mathrm{fp}}}{2m + \delta_m}.$$

The Alfvén couplings of interest can then be categorized as indicated in Table I. Further information and original references where these modes were identified can be found in Ref. 9. Of these modes, only the HAE and MAE are unique to stellarators. The HAE will generally be more common than the MAE for the configurations analyzed in this paper.

Downloaded 27 Jan 2004 to 160.91.248.206. Redistribution subject to AIP license or copyright, see http://ojps.aip.org/pop/popcr.jsp

TABLE I. Nomenclature and categories of Alfvén coupling of interest for stellarators.

Abbreviated name	Name	δ_m	δ_n
GAE	Global Alfvén eigenmode	0	0
TAE	Toroidal Alfvén eigenmode	± 1	0
EAE	Elliptical Alfvén eigenmode	± 2	0
NAE	Noncircular Alfvén eigenmode	$\lvert\delta_m\rvert \geqslant 3$	0
MAE	Mirror Alfvén eigenmode	0	$\pm 1, \pm 2, \ldots$
HAE	Helical Alfvén eigenmode	$\lvert\delta_m\rvert \geqslant 1$	$\pm 1, \pm 2, \ldots$

III. APPLICATION OF STELLGAP TO HIGH ASPECT RATIO STELLARATORS

We first apply the STELLGAP code to several discharges from the W7-AS (Wendelstein 7–Advanced Stellarator) device. Experimental results from these discharges have been previously published[10] and they are chosen to indicate the rather significant range of Alfvén continuum structures that can be accessed even within a single stellarator through the variation of its rotational transform profile.

We first consider very low shear profiles that lead to simple Alfvén continuum structures in which a single helicity mode is dominant. At least for the lowest toroidal mode numbers, this will preclude toroidally or helically coupled gaps. The only Alfvén gaps that remain are the global Alfvén eigenmode gaps (GAE) that occur below the minima of the lowest Alfvén continua and which are present even in cylindrical equilibria. These were some of the first energetic particle driven Alfvén instabilities observed in stellarator configurations.[4] A tyical case where such modes have been observed is W7-AS discharge #40173. Here the rotational transform profile varied from around 0.35 at the magnetic axis to 0.34 at the edge. In Fig. 2(a) we plot the Alfvén continua for this case, using the toroidal/poloidal mode distribution: $n=-9$ ($m=0$ to 32), $n=-6$ ($m=0$ to 22), $n=-4$ ($m=0$ to 15), $n=-1$ ($m=0$ to 10), $n=1$ ($m=0$ to 10), $n=4$ ($m=0$ to 15), $n=6$ ($m=0$ to 22) and $n=9$ ($m=0$ to 32). The central ion density was 6.6×10^{19} m^{-3}. As may be seen, there is no coupling between the different toroidal modes here that would lead to an HAE/MAE gap structure. The lowest $n=1$ mode continuum, however, does have a nonzero minimum due to the fact that the rational transform value of 0.33 was not present in the iota profile. Alfvén frequency activity ($\sim$16 kHz) was measured[10] slightly below this minimum. In the adjacent Fig. 2(b) we plot only this lowest order $n=1$, $m=3$ continuum based on cylindrical, axisymmetric tokamak and stellarator equilibrium models. As may seen, the tokamak and stellarator continua are quite similar; this is due to the fact that the GAE continua are not produced directly by equilibrium couplings (as are the TAE/HAE modes), but rather by the existence of a nonzero minimum in the continuum curve. For this reason, they are not as sensitive to the form of the equilibrium model as the other Alfvén modes; this expectation motivated the toroidally symmetric models that were used in the earlier simulations of these GAE modes.[21]

The Alfvén continuum structure is next calculated for discharge 42 873; in this case Alfvén activity was observed[10]

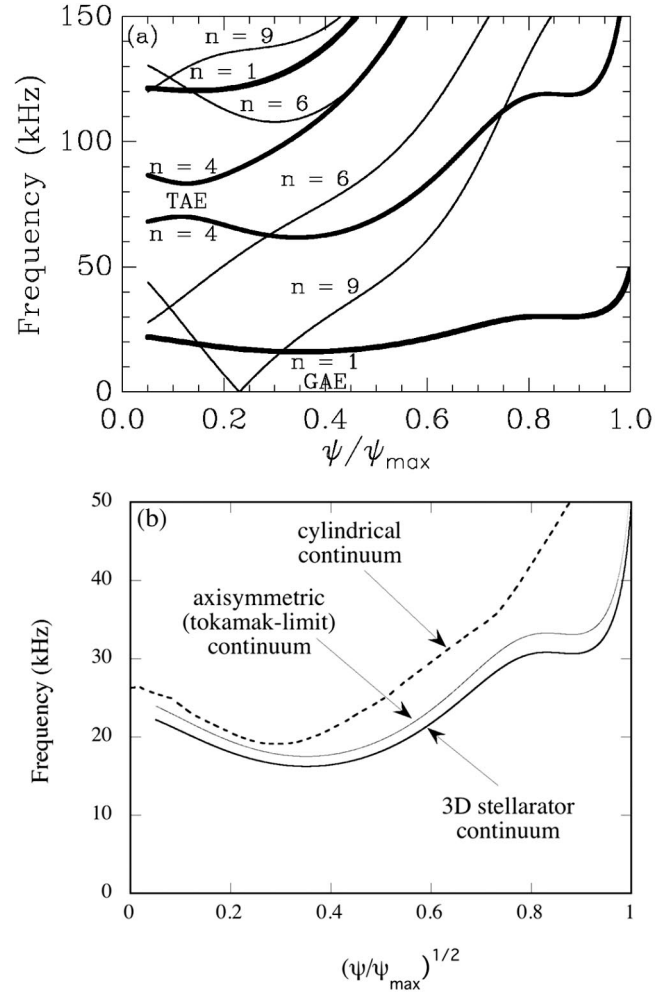

FIG. 2. (a) Continuum gap structure for W7-AS low shear case #40173, and (b) comparison of the lowest frequency $n=1$ continuum based on cylindrical, axisymmetric and stellarator equilibrium models.

for a frequency band of around 35–50 kHz. The rotational transform profile had relatively strong shear induced by the presence of a high bootstrap current that was compensated by an externally driven inductive current. Transform and ion density profiles appropriate to this discharge have been used in the continuum calculation. The transform varied from 0.11 at the magnetic axis to 0.34 at the edge. In Fig. 3(a), the Alfvén gap structure is displayed over the full cross section based upon a toroidal/poloidal mode distribution of $n=-9$ ($m=0$ to 150), $n=-6$ ($m=0$ to 55), $n=-4$ ($m=0$ to 50), $n=-1$ ($m=0$ to 20), $n=1$ ($m=0$ to 20), $n=4$ ($m=0$ to 50), $n=6$ ($m=0$ to 55) and $n=9$ ($m=0$ to 150). The central ion density was 3.6×10^{19} m^{-3}. All of the lower frequency gaps in this figure are TAE gaps; i.e., they involve only single toroidal mode number. Also, these gaps involve only m,n modes with positive helicity (i.e., $m>0$ and $n>0$). The next several bands of gaps above these are EAE gaps which again involve single toroidal mode number couplings. In Fig. 3(b) we zoom in on the region inside the rectangular box in Fig. 3(a) where HAE/MAE couplings are present and use varying linewidths to indicate the dominant toroidal mode numbers for each continua. As can be seen, at these higher

Downloaded 27 Jan 2004 to 160.91.248.206. Redistribution subject to AIP license or copyright, see http://ojps.aip.org/pop/popcr.jsp

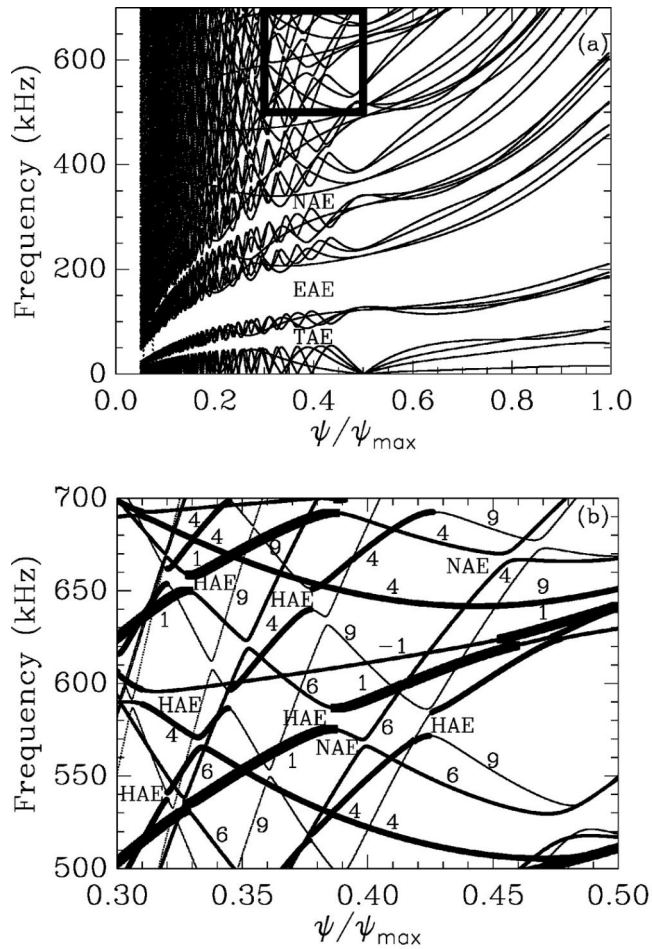

FIG. 3. (a) Continuum gap structure for W7-AS case #42873, and (b) zooming in on the region indicated by the boxed-in region in (a). The continua are labeled with the dominant toroidal mode number of the E_ψ eigenfunction and coded by line width.

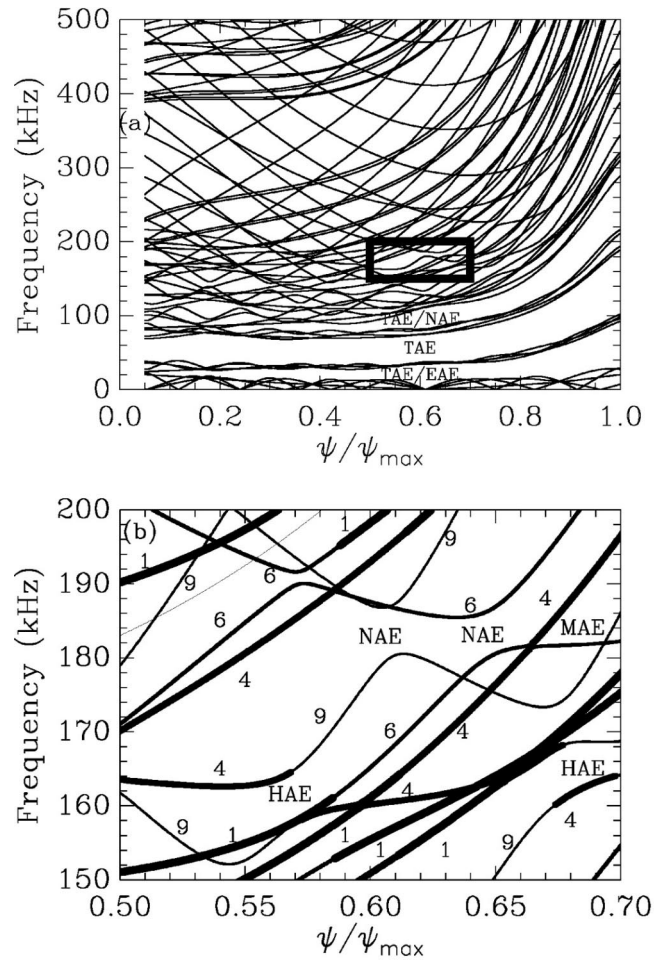

FIG. 4. (a) Continuum gap structure for W7-AS case #43348, and (b) zooming in on the region indicated by the boxed-in region in (a). The continua are labeled with the dominant toroidal mode number of the E_ψ eigenfunction and coded by line width.

frequencies, there are clearly a variety of gaps present that involve Alfvén couplings between different toroidal mode numbers.

The third W7-AS discharge we consider is #43348. In this case the rotational transform profile had a tokamak-like shear, varying from 0.39 in the center to 0.31 at the edge and bands of burstlike Alfvénic activity were observed at ~35–40 kHz, 50–60 kHz, 85–100 kHz, 130–150 kHz and 210–240 kHz. In Fig. 4(a) we plot the Alfvén continua over the full radius based on a toroidal/poloidal mode distribution of $n=-9$ ($m=0$ to 40), $n=-6$ ($m=0$ to 22), $n=-4$ ($m=0$ to 15), $n=-1$ ($m=0$ to 15), $n=1$ ($m=0$ to 15), $n=4$ ($m=0$ to 15), $n=6$ ($m=0$ to 22) and $n=9$ ($m=0$ to 40). The central ion density was 1.1×10^{20} m^{-3}. Again, the lower two gaps at ~20 kHz and 50 kHz are TAE gaps, involving only poloidal couplings, at a fixed toroidal mode number. However, as one goes to somewhat higher frequencies, as shown in Fig. 4(b), couplings between continua of different toroidal mode numbers begin inducing HAE/MAE gaps.

We next give an example of the gap structure for the LHD (Large Helical Device) torsatron to show how the gap structure changes for a higher field period stellarator. This case is not intended to correspond to any particular LHD discharge, although various types of Alfvén activity have been observed on this device.[7] Here an ion density profile that varies as $1-(\psi/\psi_{\rm edge})$ has been assumed with a central ion density of 1×10^{20} m^{-3} and the ion species taken as deuterium. The rotational transform profile varies from 0.34 at the magnetic axis to 1.37 at the plasma edge. In Fig. 5(a) we plot the Alfvén continua over the full radius based on a toroidal/poloidal mode distribution of $n=-11$ ($m=0$ to 35), $n=-9$ ($m=0$ to 32), $n=-1$ ($m=0$ to 10), $n=1$ ($m=0$ to 10), $n=9$ ($m=0$ to 32), and $n=11$ ($m=0$ to 35). The lowest order gap (running from about 50 kHz to >500 kHz at the edge) is produced by TAE couplings and there are no gaps that involve couplings between different toroidal mode numbers until one looks at higher frequencies and near the edge of the device. Such HAE/MAE gaps that couple different toroidal modes are shown in Fig. 5(b).

IV. APPLICATION OF STELLGAP TO LOW ASPECT RATIO STELLARATORS

Next, we calculate the continuum gap structure for several recently developed low aspect ratio stellarator designs.

Downloaded 27 Jan 2004 to 160.91.248.206. Redistribution subject to AIP license or copyright, see http://ojps.aip.org/pop/popcr.jsp

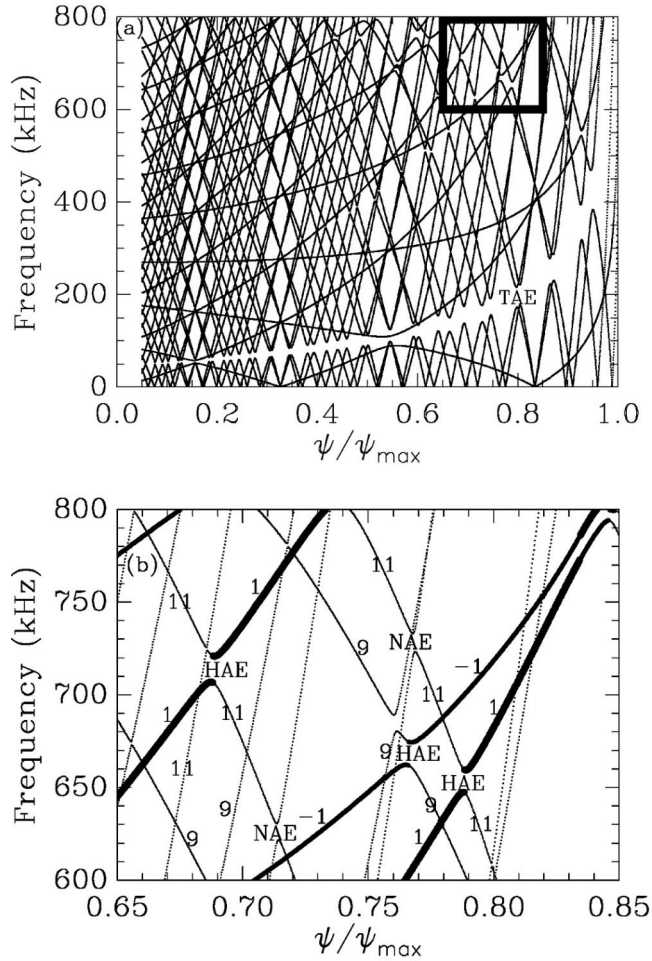

FIG. 5. Continuum gap structure for $n=1$ mode family in LHD, and (b) zooming in on the region indicated by the boxed-in region in (a). The continua are labeled with the dominant toroidal mode number of the E_ψ eigenfunction and coded by line width.

Compact stellarators can have substantially different Alfvén continuum structures than high aspect ratio stellarators for two reasons. First, the low aspect ratio results in much stronger couplings due to the significantly broader Fourier spectra of the equilibrium quantities than is the case for the high aspect ratio configurations. Second, low aspect ratio devices generally are designed with fewer field periods than high aspect ratio devices (typically the ratio $R_0/\langle a\rangle N_{\rm fp}$ is kept constant). Since the stellarator toroidal mode families are separated by $N_{\rm fp}$, the number of field periods (i.e., $n=\pm n_0$, $\pm n_0 \pm N_{\rm fp}$, $\pm n_0 \pm 2N_{\rm fp}$, etc.) low field period devices have a more densely packed set of toroidal mode numbers. This tends to induce helically induced Alfvén gaps at lower frequencies than is the case for the equivalent higher aspect ratio devices. Also, more cross-linking between the toroidal and helical gaps can be present.

We first calculate continua for a typical QPS (Quasi Poloidal Stellarator) device.[22] The equilibrium considered here was known as the qps1105 configuration and has an aspect ratio of $A=2.7$ and 2 field periods. The QPS has been optimized so that its $|B|$ spectrum in Boozer coordinates is dominated by poloidally symmetric components with $m=0$, $n\neq 0$. In Fig. 6(a) the Alfvén continua for the $n=1$ mode family are plotted with color coding used to indicate the dominant toroidal mode number of the eigenfunction.

Here we have assumed an ion density profile that goes as $1-(\psi/\psi_{\rm edge})^2$ with a central ion density of 1×10^{20} m^{-3} and the ion species taken as deuterium. The rotational transform profile varies from 0.19 at the magnetic axis to 0.27 at the plasma edge. We have used a toroidal/poloidal mode distribution of $n=-11$ ($m=1$ to 70), $n=-9$ ($m=1$–60), $n=-7$ ($m=1$–55), $n=-5$ ($m=1$ to 50), $n=-3$ ($m=1$ to 35), $n=-1$ ($m=1$ to 15), $n=1$ ($m=1$ to 15), $n=3$ ($m=0$ to 35), and $n=5$ ($m=0$ to 50), $n=7$ ($m=0$ to 55), $n=9$ ($m=0$ to 60), $n=11$ ($m=0$–70). Except for the lower continuum lines, most of the continuum gaps involve HAE/MAE couplings (i.e., modes with different m and n numbers are coupled). The presence of helically coupled gaps is evidenced by continua in Fig. 6(a) that change color as one follows them outward in flux. Such gaps generally occur at lower frequencies and closer to the magnetic axis than for either of the large aspect ratio W7-AS or LHD devices. The open gap region that runs from about 20 to 100 kHz near the magnetic axis (i.e., $\psi/\psi_{\rm max}=0$) and the $n=11$ gaps below 200 kHz involve predominantly only toroidal Alfvén couplings.

Next, in Fig. 6(b) the continuum gap structure is calculated for a compact configuration[23] that has quasi-toroidal symmetry. This device is known as the LI383 configuration and was one of the previous reference configurations considered for the proposed NCSX experiment.[24] This configuration has an aspect ratio of $A=4.4$ and 3 field periods. Quasi-toroidal symmetry implies that the $|B|$ spectrum in Boozer coordinates is dominated by components with $m\neq 0$, $n=0$ (i.e., toroidal symmetry).

Although $|B|$ in Boozer coordinates for this device has a symmetry that is close to that of a tokamak, the metric elements do not possess this symmetry. As a result, the Alfvén continua are not the same as for the equivalent tokamak device. Here we have used a toroidal/poloidal mode distribution of $n=-8$ ($m=1$ to 55), $n=-7$ ($m=1$ to 45), $n=-5$ ($m=1$ to 35), $n=-4$ ($m=1$ to 30), $n=-2$ ($m=1$ to 20), $n=-1$ ($m=1$ to 15), $n=1$ ($m=0$ to 15), $n=2$ ($m=0$ to 20), $n=4$ ($m=0$ to 30), $n=5$ ($m=0$ to 35), $n=7$ ($m=0$ to 45), $n=8$ ($m=0$ to 55). An ion density profile that goes as $1-(\psi/\psi_{\rm edge})^2$ has been used with a central ion density of 1×10^{20} m^{-3} and the ion species taken as deuterium. The rotational transform profile varies from 0.4 at the magnetic axis to 0.67 at the plasma edge. Again, HAE/MAE-like couplings (different n) are clearly present except for some of the lower frequency continua. The primary open gap that starts from $\sim$100 to 180 kHz near the magnetic axis ($\psi/\psi_{\rm max}=0$) involves both helical and toroidal couplings.

V. CONCLUSIONS

A computational method has been developed for calculating the 3D shear Alfvén continuum for stellarators and applied over a range of aspect ratios and plasma boundary shapes. This calculation is carried out in Boozer coordinates[18] using equilibria generated by the VMEC[25] code. Calculation of the Alfvén continuum is the first step in

Downloaded 27 Jan 2004 to 160.91.248.206. Redistribution subject to AIP license or copyright, see http://ojps.aip.org/pop/popcr.jsp

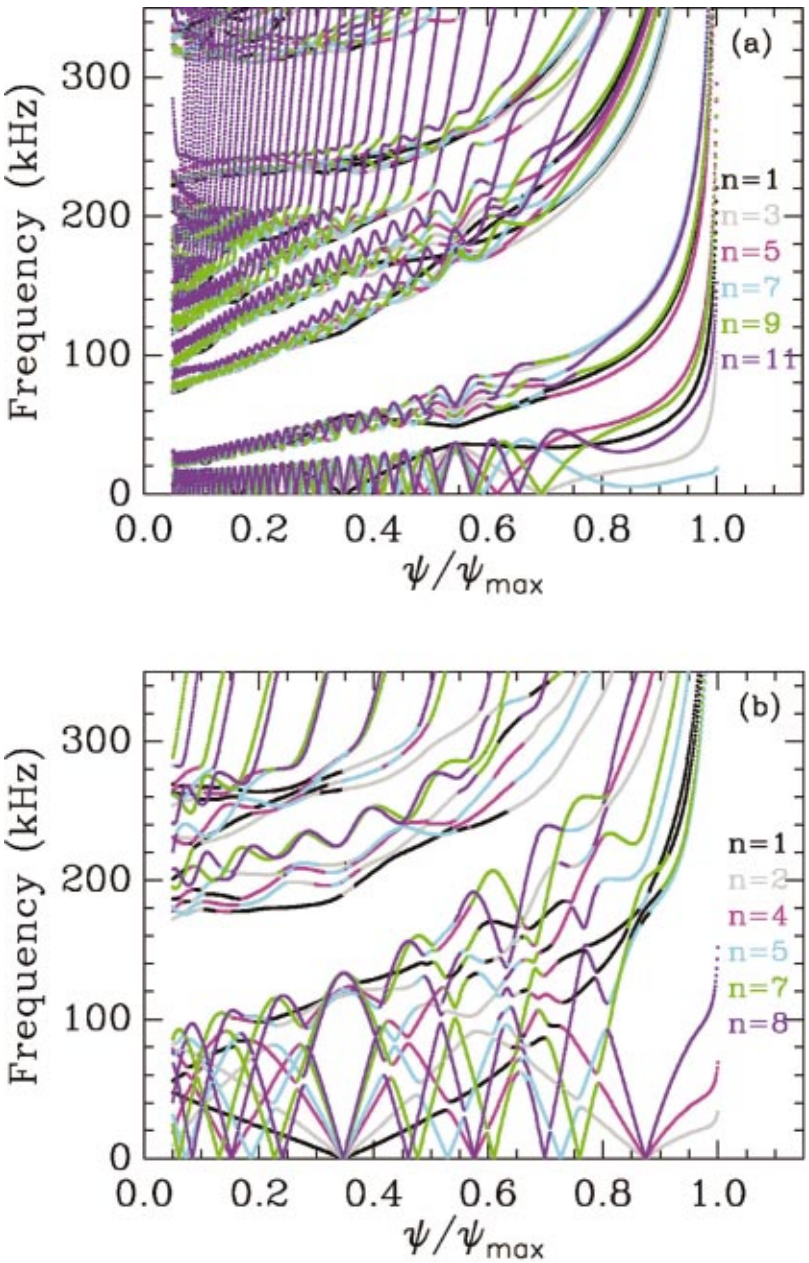

FIG. 6. (Color) (a) Continuum gap structure for the QPS device ($A=2.7, N_{fp}=2$). Color coding is used to label the dominant toroidal mode numbers with black for $n=1$, gray for $n=3$, magenta for $n=5$, light blue (cyan) for $n=7$, green for $n=9$, and violet for $n=11$; (b) continuum gap structure for the NCSX device ($A=4.4, N_{fp}=3$). Color coding is used to label the dominant toroidal mode numbers with black for $n=1$, gray for $n=2$, magenta for $n=4$, light blue (cyan) for $n=5$, green for $n=7$, and violet for $n=8$.

addressing the stability of such modes in stellarators in the presence of fast ion components. In the future, we expect to extend the above methods to calculate the mode structure of the discrete modes lying in the continuum gaps and then to examine their stability. It is also expected that a reduced version of the model presented here can be used as a stellarator optimization target to search for configurations that could suppress fast ion destabilized Alfvén modes through continuum damping effects.

We find that while stellarators still possess a certain component of the TAE gap structures that are present in axisymmetric devices, they also contain a large number of Alfvén gaps that involve helical couplings. In addition, stellarators offer a wider variation of continuum structures than is characteristic of tokamaks. These continua are more complex in stellarators due to the presence of both poloidal and toroidal couplings. For large aspect ratio stellarators, the Alfvén gaps that involve helical couplings generally occur at higher frequencies than the TAE gaps and often in the outer regions of the plasma. For compact stellarators, the helical gaps are found at lower frequencies and are more strongly cross-linked with the TAE gaps. Also, for both of the compact stellarator examples presented here, at least one open gap region has been present that persists across most of the minor radius. A unique feature of low aspect ratio devices is the larger width of this primary (i.e., lowest frequency) gap as compared to larger aspect ratio devices.

Due to the more complex continuum structures and the larger number of closely spaced Alfvén gaps, it is expected that a higher degree of temporal and spatial resolution will be required to adequately analyze the destabilization and damping of these modes in stellarators than has been the case for tokamaks. Compact stellarators introduce strong equilibrium couplings and closer spacing ($\Delta n = N_{fp}$) between adja-

Downloaded 27 Jan 2004 to 160.91.248.206. Redistribution subject to AIP license or copyright, see http://ojps.aip.org/pop/popcr.jsp

cently coupled toroidal modes since these devices are typically designed with a low number of field periods ($N_{fp} = 2-3$). This characteristic may lead to stronger continuum damping of these modes in compact stellarators.

ACKNOWLEDGMENTS

Work supported by U.S. Department of Energy under Contract No. DE-AC05-00OR22725 with UT-Battelle, LLC. The calculations in this paper have been carried out using both the resources of the National Energy Research Scientific Computing Center and the Lawrence Berkeley National Lab and the Center for Computational Sciences at Oak Ridge National Lab.

[1] C. Z. Cheng and M. S. Chance, Phys. Fluids **29**, 3695 (1986).
[2] G. Y. Fu and J. W. Van Dam, Phys. Fluids B **1**, 1949 (1989).
[3] N. Nakajima, C. Z. Cheng, and M. Okamoto, Phys. Fluids B **4**, 1115 (1992).
[4] A. Weller, D. A. Spong, R. Jaenicke, A. Lazaros, F. P. Penningsfeld, S. Sattler, W7-AS Team, and NBI Group, Phys. Rev. Lett. **72**, 1220 (1994).
[5] C. Nührenberg, Phys. Plasmas **6**, 137 (1999).
[6] N. Nakajima and Y. Nakamura, J. Plasma Fusion Res. **75**, 556 (1999).
[7] K. Toi, M. Takechi, M. Isobe *et al.*, Nucl. Fusion **40**, 1349 (2000).
[8] A. Könies, Phys. Plasmas **7**, 1139 (2000).
[9] Ya. I. Kolesnichenko, V. V. Lutsenko, H. Wobig, Yu. V. Yakovenko, and O. P. Fesenyuk, Phys. Plasmas **8**, 491 (2001).
[10] A. Weller, M. Anton, J. Geiger, M. Hirsch, R. Jaenicke, A. Werner, W7-AS Team, C. Nührenberg, E. Sallander, and D. A. Spong, Phys. Plasmas **8**, 931 (2001).
[11] A. Fasoli, D. Borba, C. Gormezano *et al.*, Plasma Phys. Controlled Fusion **39**, B287 (1997); also see J. P. Goedbloed, H. A. Holties, S. Poedts, G. T. A. Huysmans, and W. Kerner, *ibid.* **35**, B277 (1993).
[12] N. J. Fisch and M. C. Herrmann, Nucl. Fusion **35**, 1753 (1995).
[13] R. Betti and J. P. Freidberg, Phys. Fluids B **3**, 1865 (1991).
[14] M. N. Rosenbluth, H. L. Berk, D. M. Lindberg, and J. W. Van Dam, Phys. Rev. Lett. **68**, 596 (1992); F. Zonca and L. Chen, *ibid.* **68**, 592 (1992).
[15] D. A. Spong, B. A. Carreras, and C. L. Hedrick, Phys. Fluids B **4**, 3316 (1992).
[16] S. P. Hirshman, D. A. Spong, J. C. Whitson *et al.*, Phys. Plasmas **6**, 1858 (1999); G. H. Neilson, A. H. Reiman, M. C. Zarnstorff *et al.*, *ibid.* **7**, 1911 (2000).
[17] A. Salat and J. A. Tataronis, Phys. Plasmas **8**, 1200 (2001); **8**, 1207 (2001).
[18] A. H. Boozer, Phys. Fluids **24**, 1999 (1981).
[19] C. Schwab, Phys. Fluids B **5**, 3195 (1993).
[20] Engineering and Scientific Subroutine Library for AIX Guide and Reference, 5765-C42, Document Number SA22-7272-03, Copyright IBM Corp., 1997–2001, International Business Machines Corporation, 55JA, Mail Station P384, 2455 South Road, Poughkeepsie, NY 12601-5400.
[21] D. A. Spong, B. A. Carreras, C. L. Hedrick, J.-N. Leboeuf, and A. Weller, *Proceedings of the Fifteenth International Conference on Plasma Physics and Controlled Nuclear Fusion Research, Seville, Spain, 1994* (International Atomic Energy Agency, Vienna, 1994), Vol. 3, p. 567.
[22] D. A. Spong, S. P. Hirshman, L. A. Berry *et al.*, Nucl. Fusion **41**, 711 (2001).
[23] A. Reiman, L. Ku, D. Monticello *et al.*, Phys. Plasmas **8**, 2083 (2001).
[24] G. H. Neilson, M. C. Zarnstorff, L. P. Ku *et al.*, "Physics considerations in the design of NCSX," Princeton Plasma Physics Laboratory Report No. PPPL-3753, UC-70, October 2002.
[25] S. P. Hirshman and J. C. Whitson, Phys. Fluids **26**, 3553 (1983).

Downloaded 27 Jan 2004 to 160.91.248.206. Redistribution subject to AIP license or copyright, see http://ojps.aip.org/pop/popcr.jsp